September 20, 2013

# Non-Born–Oppenheimer molecular dynamics of the spin-forbidden reaction $O(^3P) + CO(X^1\Sigma^+) \sim> CO_2(\tilde{X}^1\Sigma_g^+)$

Ahren W. Jasper[a]

*Combustion Research Facility, Sandia National Laboratories, Livermore, CA 94551, USA*

Richard Dawes[b]

*Missouri University of Science and Technology, Rolla, MO 65409, USA*

**Abstract**

The lowest-energy singlet (1 $^1$A') and two lowest-energy triplet (1 $^3$A' and 1 $^3$A") electronic states of $CO_2$ are characterized using dynamically-weighted multireference configuration interaction (dw-MRCI+Q) electronic structure theory calculations extrapolated to the complete basis set (CBS) limit. Global analytic representations of the dw-MRCI+Q/CBS singlet and triplet surfaces and of their CASSCF/aug-cc-pVQZ spin-orbit coupling surfaces are obtained via the interpolated moving least squares (IMLS) semiautomated surface fitting method. The spin-forbidden kinetics of the title reaction is calculated using the coupled IMLS surfaces and coherent switches with decay of mixing (CSDM) non-Born–Oppenheimer molecular dynamics. The calculated spin-forbidden association rate coefficient (corresponding to the high pressure limit of the rate coefficient) is 7–35x larger at 1000–5000 K than the rate coefficient used in many detailed chemical models of combustion. A dynamical analysis of the multistate trajectories is presented. The trajectory calculations reveal direct (nonstatistical) and indirect (statistical) spin-forbidden reaction mechanisms and may be used to test the suitability of transition-state-theory-like statistical methods for spin-forbidden kinetics. Specifically, we consider the appropriateness of the "double passage" approximation, of assuming statistical distributions of seam crossings, and of applications of the unified statistical model for spin-forbidden reactions.

[a]Electronic mail: ajasper@sandia.gov

[b]Electronic mail: dawesr@mst.edu

## I. Introduction

The spin-forbidden oxidation of CO to $CO_2$ by ground-state (triplet) atomic oxygen O

$$O(^3P) + CO(X^1\Sigma^+)\ (+M) \longrightarrow CO_2(\tilde{X}^1\Sigma_g^+)\ (+M)\ , \qquad (1)$$

has been identified as important in some combustion systems (particularly at high pressures), where it competes with the oxidation of CO by OH, $N_2O$, etc.[1] Reaction 1 is a sink for O atoms and can therefore inhibit chain branching. Few theoretical studies of the spin-forbidden kinetics or dynamics of this system have appeared previously. Troe[2] calculated the high-pressure association rate coefficient ($k_{1\infty}$), and Westmoreland et al.[3] fit experimental falloff kinetics to the results of QRRK calculations. These expressions (with some adjustments[1]) are used in many detailed chemical models for combustion.[4,5]

Hwang and Mebel[6] characterized the energetics of the lowest-energy singlet and lowest-energy triplet surfaces of $CO_2$ using several levels of electronic structure theory. They identified two spin-forbidden mechanisms for the oxidation of CO by O: a "direct" mechanism via a singlet–triplet curve crossing associated with a collinear geometry and an extended incipient C–O bond distance

$$O + CO \sim\!> CO_2 \qquad \text{(direct)}$$

("$\sim\!>$" denotes a spin-forbidden event) and an "indirect" mechanism where a short-lived triplet complex $^3CO_2$ is formed and quenched via a singlet–triplet curve crossing associated with a bent geometry, i.e.,

$$O + CO \rightleftarrows {}^3CO_2 \sim\!> CO_2\,. \qquad \text{(indirect)}$$

Based on the energetics and spin–orbit coupling strengths calculated at the linear and bent crossing seams both mechanisms were suggested to be important,[6] but no dynamics or kinetics calculations were carried out.

Analytic potential energy surfaces for the three lowest triplet states of $CO_2$ based on multireference perturbation theory calculations were developed and used in adiabatic (i.e., uncoupled, single state) classical trajectory calculations of hyperthermal scattering,[7,8] with favorable comparisons with experimental results. Singlet potential energy surfaces and spin-forbidden multistate dynamics were not considered in Refs. 7 and 8. Six singlet states of $CO_2$ were recently characterized in detail,[9] but no triplet states or spin-forbidden dynamics were

considered. In earlier work,[10] excited singlet and triplet states of $CO_2$ were characterized at $C_{2v}$ geometries using multireference methods.

Experimental kinetics studies of the thermal decomposition of $CO_2$ (reaction –1) have been carried out at high temperatures and low pressures.[11,12,13] Under these conditions, the $CO_2$ decomposition reaction is 2nd order (i.e., reaction –1 is in the low-pressure $CO_2$ + M limit), and in this limit the unimolecular decomposition rates are determined by the rates of collisional energy transfer[14,15] and not by the spin-forbidden dynamics. There has been some experimental work at elevated pressures, with decomposition studied at pressures as high as 250 atm[16,17] and association measured up to 24 atm.[18] In both of these studies, extrapolations to higher pressures resulted in limiting values consistent with Troe's value of $k_{1\infty}$. However, even at the highest pressures experimentally probed, the reaction was observed to be consistent with (or close to) a second order (low-pressure-limit) picture. We are not aware of any experimental studies that have directly probed the high-pressure limit spin-forbidden kinetics of reaction 1 in either the forward or reverse direction.

Finally, we note that the photodissociation of $CO_2$ to the spin-forbidden products O + CO has been studied by several groups.[19,20,21,22,23] This process is thought to involve spin-forbidden transitions out of a photoexcited singlet state. These dynamics therefore may not be directly relevant to the present study, which considers coupling of the triplet states of $CO_2$ to the ground-state singlet state.

Here we present a detailed electronic structure and spin-forbidden molecular dynamics study of reaction 1, and its high-pressure limit rate coefficient ($k_{1\infty}$) is reported from 1000–5000 K. Pressure-dependent kinetics and low-pressure-limit kinetics are not considered. In the high-pressure limit, the kinetics of reaction 1 is determined principally by its spin-forbidden dynamics. While electronically adiabatic kinetics is readily and accurately calculated via transition state theory[24,25] (TST) and other methods, fewer strategies exist for accurately predicting electronically nonadiabatic (including spin-forbidden) kinetics. Here we employ multistate (also called "electronically nonadiabatic" or "non-Born–Oppenheimer") trajectories[26,27] and in particular the coherent switches with decay of mixing (CSDM) method.[28] This method includes desirable features of both mean-field[29] and surface hopping[30] multistate trajectory methods, and it was found to be the most accurate of several methods included in a systematic set of tests.[27] A discussion of the expected accuracy of this approach for this system is

included. Spin-forbidden kinetics may also be characterized using statistical formulations, such as so-called "nonadiabatic transition state theory" (NA TST).[31,32] Another goal of the present work is to use the multistate trajectory results to critically evaluate some features of available electronically nonadiabatic statistical approaches.

This paper is organized as follows. In Sec. II.A, multireference quantum chemistry calculations are used to characterize three electronic states of $CO_2$ and two spin–orbit coupling surfaces. In Sec. II.B, analytic fits based on the multireference quantum chemistry methods are obtained for each of the five surfaces using the IMLS method.[33,34,35,36] In Sec. III.A, theoretical details of the present CSDM trajectory calculations are presented. In Sec. III.B, the CSDM method is used to calculate the rate coefficient for reaction 1 from 1000–5000 K. In Sec. III.C, dynamical details of the CSDM calculations are analyzed and used to infer the relative importance of the direct and indirect spin-forbidden mechanisms discussed above. Details of the trajectory calculations are also used to comment on the appropriateness of using statistical models for studying spin-forbidden reactions. Section IV is a summary. In the Appendix, the expected accuracy of the present kinetics calculations is discussed.

## II. Spin-orbit coupled potential energy surfaces

### II.A. Quantum chemistry

Reaction 1 proceeds initially on one of three triplet surfaces, and the formation of stable $CO_2$ requires a spin-forbidden transition to the ground-state singlet surface. The lowest-energy singlet ($^1$A' or S0) and the two lowest-energy triplet ($^3$A' or T1 and $^3$A" or T2) surfaces were characterized at the dw-MRCI+Q/CBS level of theory, where: three triplet and five singlet states were dynamically weighted[37,38] (dw) in the CASSCF step with a weighting range parameter of $\beta$ = 4.5 eV, the Davidson correction (+Q) was applied to the multireference configuration interaction (MRCI) energies, the complete basis set CBS limit was extrapolated using a two-point $l^{-3}$ formula[39] and the aug-cc-pVTZ and aug-cc-pVQZ basis sets, and an active space of 12 electrons in 10 orbitals (12e,10o) was used, corresponding to a nearly full valence active space (the 1*s* and 2*s* orbitals of both oxygen atoms and the 1*s* orbital of carbon were closed). The third nonreactive triplet surface is not considered here.

For small systems like $CO_2$ where a nearly full valence active space and large-basis-set CBS extrapolations can be employed, the dw-MRCI+Q/CBS method is very accurate. The

present dw-MRCI+Q/CBS stationary points energies, frequencies, and geometries are compared with experimental and past theoretical work in Table 1. The present calculated values are in excellent agreement with available experimental data,[40] with an error of only 0.3 kcal/mol for the triplet–singlet gap in atomic O and less than 0.001 Å for the CO and $CO_2$ bond distances. The calculated $CO_2$ bond energy agrees with the experimental value within its reported uncertainty after corrections for zero point energy and spin–orbit splitting. The dw-MRCI+Q/CBS method has recently been used to characterize multiple electronic states for several small systems with multireference character (e.g., BeC, CHCl, and $O_3$) with similarly excellent agreement with experimental energies, frequencies, and geometries.[41,42,43]

Spin–orbit coupling surfaces were calculated using: the Breit-Pauli Hamiltonian[44] ($\hat{H}_{\mathrm{SO}}$) as implemented in the electronic structure program Molpro,[45] the dw-CASSCF/aug-cc-pVQZ method, and the (12e,10o) active space. The two geometry-dependent spin–orbit coupling surfaces considered here are defined

$$\varepsilon_1 = \left| \left\langle {}^1A' \middle| \hat{H}_{\mathrm{SO}} \middle| {}^3A' \right\rangle \right| \tag{2a}$$

$$\varepsilon_2 = \left| \left\langle {}^1A' \middle| \hat{H}_{\mathrm{SO}} \middle| {}^3A'' \right\rangle \right|, \tag{2b}$$

where the triplet wave functions include a sum over three triplet spin-states. The magnitudes of the matrix products in eq 2 were calculated using the full Breit-Pauli Hamiltonian (i.e., including all 3 spin-states for each of the triplet states) and are invariant to the choice of representation of the triplet spin-states.

The electronic structure of the spin–orbit coupled states for the O + CO reaction is similar to that for the O + $H_2$ reaction, which has been characterized in detail by other workers.[46,47,48] Schatz et al.[46,47] showed that the full 7 × 7 Breit-Pauli Hamiltonian matrix (including the lowest-energy singlet and two lowest-energy triplet states) could be factored into a 4 × 4 subblock and 3 × 3 subblock, where only the 4 × 4 subblock contains the spin–orbit coupling matrix elements responsible for intersystem crossing. Furthermore, they showed that a unitary transformation of the triplet wavefunctions allows for an entirely real-valued representation of the Hamiltonian matrix. Here we have adopted a similar model. We have further neglected matrix elements of $\hat{H}_{\mathrm{SO}}$ between the triplet states. This simplification reduces the 4 × 4 model to a 3 × 3 one. One result of this neglect of triplet-triplet coupling is that the the atomic spin–orbit interactions that split the ${}^3P$ states of O into ${}^3P_2$, ${}^3P_1$, and ${}^3P_0$ states are not included.

The present model for $CO_2$ includes what are likely the most important nonadiabatic couplings for the O + CO reaction at the high temperatures considered here, namely those associated with spin-forbidden transitions between the triplet and singlet surfaces that occur at the singlet-triplet crossing seams. This model neglects various other nonadiabatic couplings that would complicate the dynamics but that are likely either well-approximated via simple models or else negligible. Specifically, the couplings between the three triplet states in the entrance channel are not explicitly considered, and instead it is assumed that the triplets are equally populated when they emerge from this region of the potential energy surfaces. Although there are certainly electronic transitions among the triplet states as O approaches CO, the net effect of these transitions is likely negligible at the temperatures considered here. The suitability of such a statistical model for the populations of the triplet states in the entrance channel was recently demonstrated (down to low energies) using quantum scattering calculations for O + $D_2$.[49] We have also neglected nonadiabatic couplings between the triplet surfaces. Spin–orbit-induced transitions between the triplet surfaces are unlikely to be important away from the entrance channel due to the nonzero energetic separations of the triplets for the bent $^3CO_2$ species. The present model therefore includes the assumption that population transfer between T1 and T2 is negligible. We will briefly consider the limit of fast T1/T2 quenching below.

The calculated $\varepsilon_1$ surface was found to show some sensitivity to the choice of active space. Table 2 summarizes calculated values of $\varepsilon_1$ and $\varepsilon_2$ at reference geometries near the minimum-energy geometries of the S0/T1 and S0/T2 crossing seams at several levels of theory differing in the choice of: level of correlation, basis set, active space, and state averaging strategy. The calculated values of $\varepsilon_1$ and $\varepsilon_2$ are largely insensitive to the choice of basis set, level of dynamical correlation (i.e., CASSCF or MRCI), and state averaging strategy, with the calculated spin–orbit coupling strengths differing from one another by less than ~10%. For $\varepsilon_1$, there is a significant dependence on the choice of active space, however, with the smallest active space predicting $\varepsilon_1$ = 20.6 $cm^{-1}$, which is more than a factor of two smaller than what the (12e,10o) active space predicts (46.7 $cm^{-1}$). Hwang and Mebel reported $\varepsilon_1$ = 20.3 $cm^{-1}$ using CASSCF and a full valence (16e,12o) active space; the present full valence CASSCF calculation predicts a larger value (53.4 $cm^{-1}$). The absolute difference of the largest and smallest computed values for $\varepsilon_1$ is small (only 33 $cm^{-1}$). Benchmark calculations of the splitting for ground state atomic oxygen (using CASSCF/aug-cc-pVQZ as employed here) confirm the accuracy of the

Breit-Pauli method (lowering the $^3P_2$ component by 79.3 $cm^{-1}$ in nearly exact agreement with experiment).[50,51] Nonetheless, the relative differences in the present range of computed values for $\varepsilon_1$ may be kinetically important. Spin-forbidden rates scale as $\sim\varepsilon^2$, such that an error in $\varepsilon$ of a factor of two results in a factor of four error in the spin-forbidden kinetics. We have chosen to use the (12e,10o) active space to fit the analytic coupling surfaces discussed next. At this level of theory, the S0/T1 and S0/T2 crossing seams feature spin–orbit coupling strengths with similar magnitudes.

### II.B. IMLS diabatic potential energy matrix

An analytic global representation of the 3 x 3 diabatic (or, quasidiabatic[52]) potential energy matrix

$$\mathbf{U} = \begin{pmatrix} V_{S0} & \varepsilon_1 & \varepsilon_2 \\ \varepsilon_1 & V_{T1} & 0 \\ \varepsilon_2 & 0 & V_{T2} \end{pmatrix}, \qquad (3)$$

where $V_X$ is the energy of state $X$ ($X$ = S0, T1, or T2), was obtained by fitting the results of the ab initio methods discussed in Sec. II.A using the IMLS semiautomatic fitting method.[33] The PESs were fit in Jacobi coordinates in the ranges $r_{CO}$ = [0.92, 1.42] Å, $R_{O—CO}$ = [0.8, 4.0] Å, and $\theta$ = [0, π]. The number of ab initio data included in the fits is 3057, 1477, and 1675 for the S0, T1, and T2 PESs, respectively. For all three PESs the estimated interpolation errors (randomly sampled over the geometry ranges) are ~3 $cm^{-1}$. Estimated errors are based on deviations between the fitting basis of 180 functions and a smaller basis of 138 functions. Details of the error estimation procedure have been reported previously.[33] Small test sets of ab initio data (not included in the fit) confirm the estimated error as an RMS measure. The fitting errors for some of the stationary points in Table 1 are slightly larger (<0.2 kcal/mol). Overall, the accuracy of both the quantum chemistry method and the fitting strategy is expected to be very good for the present application, as discussed in detail in the Appendix.

Contour plots of the five fitted diabatic potential surfaces are shown in Fig. 1, where $R$ is the incipient C–O bond distance and $\theta$ is the O–C–O bond angle. The remaining C–O distance was optimized. As discussed previously,[6,7] the $^3$A' (T1) and $^3$A" (T2) triplet surfaces both feature weakly bound bent $^3CO_2$ minima behind low barriers for association. These barriers (indicated

with o's in Fig. 1) have classical thresholds of 6.5 and 8.0 kcal/mol relative to O + CO for T1 and T2, respectively.

The S0/T1 and S0/T2 crossing seams are also shown in Fig. 1, and in both cases the seams separate the saddle points from the triplet wells. The minimum-energy geometry on the seam of crossings (MSX) is sometimes used to characterize spin-forbidden dynamics.[31,32] In fact, an analogy with electronically adiabatic dynamics is sometimes made, where the MSX is treated as a kind of "spin-forbidden saddle point." The MSXs are indicated by x's in Fig. 1. As reported previously,[6] the S0/T1 MSX has a geometry similar to that of the T1 $^3CO_2$ equilibrium structure with $C_{2v}$ symmetry and a smaller bond angle than that for $^3CO_2$. In contrast, the S0/T2 MSX geometry is similar to that of the T2 saddle point, with one extended CO distance and a bond angle of 122°. (We note that the second S0/T1 MSX reported previously[6] at collinear geometries is a local maximum on the crossing seam, not a local minimum. This feature can be seen in Fig. 2(b) near $R$ = 1.9 Å and $\theta$ = 180°.) One may be tempted to interpret the qualitative differences between the S0/T1 and S0/T2 MSX geometries as suggesting different spin-forbidden mechanisms, just as one often uses saddle point geometries to infer adiabatic reaction mechanisms. If the global crossing seam is considered, however, the S0/T1 and S0/T2 spin-forbidden mechanisms appear more similar to one another, as both seams pass near the triplet saddle points and minima. The full dimensional multistate trajectories reported in Sec. III will be used to characterize and compare the S0/T1 and S0/T2 spin-forbidden dynamics in detail.

The spin-orbit coupling strengths ($\varepsilon_1$ and $\varepsilon_2$) vary from 45–80 $cm^{-1}$ near the crossing seams, with similar magnitudes for the S0/T1 and S0/T2 seams. In the perturbative limit, spin-forbidden kinetics varies as the square of the spin-orbit coupling, such that a factor of two variation in $\varepsilon_1$ and $\varepsilon_2$ along the seams can lead to a factor of four variation in the local spin-forbidden probability.

Before the results of the dynamical calculations are presented in Sec. III, the global potential energy surfaces in Fig. 2 may be interpreted to indicate the following mechanism for reaction 1. The reaction proceeds initially with equal populations on the two triplet surfaces (and a third nonreactive triplet surface). On either reactive surface, the system first encounters an electronically adiabatic transition state associated with a triplet saddle point and an incipient bond distance of $R$ = 1.9 Å. This dynamical bottleneck focuses the reactive fraction of collisions with respect to the O–C–O bond angle $\theta$, such that the system likely first encounters the

subsequent singlet–triplet crossing seam with bond angles similar to that of the saddle point. At the crossing seam, there is some small probability for switching to the singlet surface, and a successful surface switch quickly leads to the formation of singlet $CO_2$. The system is more likely, however, to stay on the triplet surface and to encounter the shallow $^3CO_2$ well. The triplet well is not deep enough to significantly trap the system, but it may delay the system and promote multiple seam crossings. If the $^3CO_2$ species are long lived enough, one might expect a statistical distribution of seam crossings. At each seam crossing there is some small probability of switching to the singlet surface and subsequently forming $CO_2$. The spin-forbidden transition probability is approximately proportional to $\varepsilon^2$, such that the location of the seam crossing can affect the transition probability by as much as a factor of four. We may therefore identify the following direct and indirect spin-forbidden mechanisms: The "direct" spin-forbidden mechanism is associated with the first set of seam crossings and features a nonstatistical distribution at the crossing seam shaped by the preceding saddle point. The "indirect" spin-forbidden mechanism, on the other hand, is the result of sufficient equilibration in the $^3CO_2$ wells and features a statistical distribution at the crossing seam. The relative importance of these two mechanisms will be quantified in Sec. III for the present system and generally depends on the temperature or energy, the depth of the transient well, the local nonadiabatic transition probabilities, etc. These mechanisms are in the spirit of the direct and indirect mechanisms suggested earlier[6] and discussed in the Introduction, although here we associate the two mechanisms with distinct dynamical effects and not with local minima on the crossing seam.

## III. Non-Born–Oppenheimer molecular dynamics

### III.A. Theory

A variety of multistate trajectory methods have been developed that incorporate electronic state changes into molecular dynamics (classical trajectory) simulations, including the trajectory surface hopping,[30,53] spawning,[54] and decay-of-mixing[28,55] classes of methods. These methods all rely on classical trajectories to describe the nuclear motion of the system, and they differ from one another in their treatments of the electronic motion and in their schemes for coupling nuclear and electronic degrees of freedom. While the term non-Born–Oppenheimer molecular dynamics (NBO MD) could be used to refer to any of these methods generally, we have used this term in the past to describe the methods we have developed. A series of

systematic studies of the accuracy of several NBO MD methods was carried out,[56,57,58] and the results have been reviewed.[27,59,60] Here we primarily consider the coherent switches with decay of mixing (CSDM) NBO MD method.[28]

CSDM trajectories are propagated on a mean-field[29] potential energy surface, which is a weighted average of the diabatic potential energy surfaces. Although CSDM calculations may be carried out in adiabatic, diabatic, or mixed representations, the diabatic representation given by eq 3 was used exclusively in the present work. This choice is supported by past studies showing that the most accurate representation for semiclassical trajectory methods is the one in which coupling is minimized.[61] In many mean-field nonadiabatic trajectory calculations, the weights of each diabatic surface are given by the electronic state populations and coherences, which are obtained by integrating the solution to the time-dependent electronic Schrödinger equation along each trajectory.[26] In the CSDM method, these weights are modified to include electronic decoherence[62,63,64] via additional de-mixing terms with first-order de-mixing times given by[55]

$$\tau = \frac{\hbar}{\Delta V}\left(1+\frac{E_0}{T_s}\right), \qquad (4)$$

where $\Delta V$ is difference in the diabatic electronic energies of the diabatic state toward with the system is de-mixing and some other state, $E_0$ is a parameter, and $T_s$ is the kinetic energy associated with the component of the momentum where energy is being added or removed as the trajectory de-mixes. De-mixing forces each CSDM trajectory into a quantized electronic state in the absence of coupling, which also causes the mixed electronic state of a CSDM trajectory to decohere as the same rate. The electronic state toward which the trajectory de-mixes is determined by a fewest-switches[26] criterion based on a locally coherent set of electronic state populations.

The CSDM method may be thought of as intermediate of surface hopping and mean field methods. Like surface hopping trajectories, CSDM trajectories are electronically quantized away from regions of coupling and therefore share the desirable features of being able to explore low-probability events, having physical internal energy distributions, etc.[30] Unlike surface hopping trajectories, however, CSDM trajectories do not feature sudden momentum changes and the associated problem of frustrated hops.[57,65] Furthermore, the mean-field nonadiabatic dynamics in regions of coupling leads to predicted reaction probabilities and internal energy distributions that are more accurate and less dependent on the choice of electronic representation than surface

hopping trajectories.[27,59] The CSDM method was shown to be the most accurate of several multistate trajectory methods in tests against quantum mechanical results for atom–diatom scattering reactions and featuring several different couplings types and strengths.[27,59]

The CSDM method was initially employed with $E_0$ = 0.05–0.2 $E_h$ (1 $E_h$ = 27.21 eV), and the results were not overly sensitive to this parameter for small systems.[28] A recent study showed some sensitivity for larger systems.[66] Here we choose $E_0$ by comparing $\tau$ from eq 4 with semiclassical decoherence times $\tau_{SC}$ calculated via a model based on the short-time behavior of minimum-uncertainty wave packets.[67] Specifically, for several values of $E_0$, the de-mixing rates $\tau^{-1}$ were averaged over the spin-forbidden interaction regions encountered by a small batch of CSDM trajectories. The interaction regions were defined as the segments of the trajectories immediately following a seam encounter and then preceding a local minimum in the magnitude of the vector (or gradient) nonadiabatic coupling[26] strength. These regions include the majority of the important spin-forbidden dynamics; outside of these regions, the trajectories largely behave adiabatically. For a CSDM ensemble at 4000 K, setting $E_0$ = 0.01 $E_h$ resulted in interaction-region-averaged de-mixing rates that agreed with those of the semiclassical model within 3%, whereas values of $E_0$ = 0.1, 0.02, and 0.005 $E_h$ resulted in interaction-region-averaged de-mixing rates that differed from the averaged semiclassical decoherence rates by –60%, –20%, and +25%, respectively. We note that in general the CSDM de-mixing times are somewhat larger than $\tau_{SC}$ for short decoherence times and are somewhat shorter than $\tau_{SC}$ for long decoherence times. Despite this (weak) inverse correlation, with $E_0$ set to 0.01 $E_h$ both models predict similarly fast decoherence (e.g., typically $\tau_{SC}$ < 5 fs), as expected for the localized spin-forbidden dynamics considered here.

CSDM trajectories were initiated in either the T1 or T2 electronic state. While in principle a trajectory initiated in the T1 state may eventually couple to the T2 state (via the S0 state) and vice-versa, this effect was found to be was negligible. Reduced 2 x 2 diabatic representations

$$\mathbf{U}_{Tx} = \begin{pmatrix} V_{S0} & \varepsilon_x \\ \varepsilon_x & V_{Tx} \end{pmatrix}, \tag{5}$$

where $x$ = 1 or 2, were therefore used in many of the trajectory simulations. Spin-free or "valence" nonadiabatic coupling[68] for the representations defined by eqs 3 and 5 is neglected; i.e., all of the nonadiabatic dynamics is assumed to arise from the spin-orbit interactions in eq 2.

The initial rovibrational state of CO was selected *classically* from a thermal distribution at temperature $T$ by sampling the initial coordinates and momenta evenly in time from isolated CO trajectories subject to an Andersen thermostat.[69] The impact parameter $b$ was selected evenly in $b^2$ from $0–b_{max}^2$ ($b_{max}$ = 2 Å), with the relative collision energy selected from a thermal distribution and an initial O–CO center-of-mass distance of 4 Å. These sampling limits were confirmed to be suitable for the high temperatures considered here. We emphasize that the present prescription for initial conditions is entirely classical. Quasiclassical[70,71] or Wigner[72] initial conditions, particularly for rovibrational-state-selected collisions, are often used when performing classical trajectories. Here we are not concerned with state-selected chemistry but instead with high temperature kinetics. Therefore, we choose to calculate "classical" rate coefficients (these rate coefficients are of course not *entirely* classical, as they include nonclassical spin-forbidden transitions) and then to estimate the effect of quantized vibrations via corrections to the partition functions and threshold energies. For this system, these corrections are negligible above 2000 K and are small at 1000 K, as detailed in the Appendix.

Product channels $\alpha$ were assigned to each trajectory by monitoring the two C–O distances and the electronic state populations, with $\alpha$ = "S" for the spin-forbidden singlet $CO_2$ product and $\alpha$ = "E" for the O exchange reaction to give $^3O$ + CO. A few trajectories produced the $^1O$ + CO product channel at high temperatures, but this negligible fraction is not considered here. Bimolecular products were identified when one C–O bond distance exceeded 4 Å, and the molecular product $CO_2$ was identified when the incipient bond distance was shorter than 1.3 Å *and* the instantaneous electronic state population for the singlet was greater than 0.99.

Using standard formulas, the bimolecular reaction cross section for product channel $\alpha$ is[70,71]

$$\sigma_\alpha^s(T) = \pi b_{max}^2 F_\alpha^s(T), \qquad (6)$$

where $s$ = T1 or T2 and labels the initial electronic state, and $F_\alpha^s$ is the fraction of trajectories that finish the trajectory simulation in the $\alpha$ product channel. The related rate coefficients are[70,71]

$$k_\alpha^s(T) = g_e \sqrt{\frac{8k_B T}{\pi\mu}} \sigma_\alpha^s, \tag{7}$$

where $\mu$ is the reduced mass of CO and O, and $g_e$ is the ratio of the electronic partition functions for the reactive surfaces and reactants. One-sigma uncertainties were calculated in the usual way for binned quantities.[70,71] The total rate coefficient includes contributions from both reactive triplet states:

$$k_\alpha(T) = k_\alpha^{T1} + k_\alpha^{T2}, \tag{8}$$

where $k_{1\infty}(T) \equiv k_S(T)$. In eq 8, the T1 and T2 states are assumed to be equally populated prior to reaction, which is appropriate for the temperatures considered here.

The ensembles for each temperature and each initial electronic state included 25600–51200 CSDM trajectories, such that one-sigma statistical uncertainties in the calculated rate coefficients were typically converged to better than 10%.

We also briefly consider the fewest-switches with time uncertainty[53] (FSTU) surface hopping method. This method is a modification of Tully's fewest switches method,[30] where some hopping attempts that would otherwise be frustrated[57] are instead allowed to hop by incorporating uncertainty into the hopping location. The calculations were carried using the stochastic decoherence[73] (SD) model for electronic decoherence and the "$\nabla V$" criterion.[74] The other details of the FSTU trajectories are as described above for the CSDM calculations.

### III.B. Spin-forbidden kinetics

The calculated CSDM rate coefficients for reaction 1 are shown in Fig. 2. The results were fit to the modified Arrhenius expressions

$$k_S^{T1}(T) = 1.2\times10^{-11}(T/298\,\mathrm{K})^{-0.83}\exp(-4400\,\mathrm{K}/T) \quad \mathrm{cm^3\ molecule^{-1}\ s^{-1}}, \tag{9}$$

$$k_S^{T2}(T) = 6.3\times10^{-13}\exp(-4750\,\mathrm{K}/T) \quad \mathrm{cm^3\ molecule^{-1}\ s^{-1}}, \tag{10}$$

$$k_{1\infty}(T) = 2.8\times10^{-11}(T/298\,\mathrm{K})^{-0.96}\exp(-4950\,\mathrm{K}/T) \quad \mathrm{cm^3\ molecule^{-1}\ s^{-1}}, \tag{11}$$

The present value of $k_{1\infty}(T)$ is 7–35x larger than the single existing theoretical literature value[2] for the high pressure limit of reaction 1, with larger differences at higher temperatures. These differences are outside the expected accuracy of the present approach, as discussed in the Appendix, but may not be outside the combined uncertainties of the two calculations.

In general, both reactive triplet states contribute to the total rate for reaction 1, with $k_S^{T1} / k_S^{T2} = 4$ at 2000 K and 1.4 at 5000 K. The difference in the temperature dependence of $k_S^{T1}$ and $k_S^{T2}$ can be attributed to their different spin-forbidden reaction thresholds. The submerged threshold for the S0/T1 crossing seam leads to a flat temperature dependence in $k_S^{T1}$ above 2000 K, where the spin-forbidden event is rate limiting. Below 2000 K, the adiabatic transition state associated with the T1 saddle point is rate limiting, which leads to the positive the temperature dependence observed at these temperatures. For $k_S^{T2}$, the positive S0/T2 crossing seam threshold leads to a positive temperature dependence for the entire temperature range considered here. The two spin-forbidden rates tend to similar values at high temperatures, where the effects of the different threshold energies are mitigated by the larger total energies.

As mentioned in Sec. II.A, the present model neglects direct population transfer between the triplet states. It is also interesting to consider the limit of fast population transfer between these two states. In this limit, trajectories that pass through the adiabatic transition state associated with the T2 saddle point are assumed to be quenched to T1 and then may react via the S0/T1 seam. At high temperatures, the main bottleneck on T2 is the crossing seam and fast T2/T1 population exchange would then tend to increase the total rate coefficient for reaction (by up to 30% at 5000 K). At 1000 K, the maximum effect would be to increase the total rate coefficient by 80%, but this increase is mitigated by the increased importance of the saddle point bottlenecks at low temperature.

The sensitivity of the predicted results on various parameters in the multistate trajectory method is briefly considered next. For $k_S^{T1}$(4000 K), varying the de-mixing parameter $E_0$ from 0.01 to 0.005 and 0.02 $E_h$ resulted in relative changes in the predicted rate coefficient of –13% and +18%, respectively. The weak sensitivity of the present predictions with respect to the choice of the parameter $E_0$ is encouraging; the choice of $E_0 = 0.01\ E_h$ for the results reported in Fig. 2 was motivated by comparisons with a semiclassical model for decoherence, as discussed above. Using a different model for decoherence altogether has a more significant effect on the present predictions. Specifically, the rate coefficient predicted by the FSTU surface hopping method and the stochastic decoherence (SD) model is ~4x larger than the CSDM rate coefficient reported above. Similarly large differences in CSDM and FSTU predictions were previously reported for weakly coupled systems[27,58] and may be attributed in part to the presence of

frustrated hops in the FSTU method. The present FSTU trajectories suffer significantly from frustrated hops, with nearly equal numbers of FSTU trajectories experiencing frustrated hops and classically allowed hops.

The CSDM results were confirmed be close to the perturbative limit with respect $\varepsilon_1$ and $\varepsilon_2$, with rate coefficients that scale as $\sim\varepsilon_i^2$ over entire temperature range considered here for T2 and above 2000 K for T1. For T1 at 1000 and 2000 K, the adiabatic saddle point transition state is significantly rate limiting, and so changes to the spin–orbit coupling have a small effect on the overall kinetics.

Finally, we note that symmetric exchange reactions (O' + CO → O + CO') were found to be 4–40x more likely than the spin-forbidden reactions. The calculated rate coefficients for the exchange reaction are

$$k_{\mathrm{E}}^{\mathrm{T1}}(T) = 9.5\times10^{-12}(T/298\,\mathrm{K})^{-0.39}\exp(-4300\,\mathrm{K}/T) \quad \mathrm{cm^3\ molecule^{-1}\ s^{-1}}, \qquad (12)$$

$$k_{\mathrm{E}}^{\mathrm{T2}}(T) = 2.5\times10^{-12}(T/298K)^{-0.86}\exp(-4600\,\mathrm{K}/T) \quad \mathrm{cm^3\ molecule^{-1}\ s^{-1}}, \qquad (13)$$

$$k_{\mathrm{E}}^{\mathrm{T1}}(T)+k_{\mathrm{E}}^{\mathrm{T2}}(T) = 8.5\times10^{-12}(T/298\,\mathrm{K})^{-0.65}\exp(-4200\,\mathrm{K}/T) \quad \mathrm{cm^3\ molecule^{-1}\ s^{-1}}. \qquad (14)$$

### III.C. Spin-forbidden dynamics

In this section, dynamical details of the spin-forbidden CSDM trajectories are presented, with an emphasis on quantifying the relative importance of the direct and indirect mechanisms discussed in Sec. II.B. First, we consider the extent to which the T1 and T2 $^3CO_2$ wells delay the system and promote multiple seam crossings. In the following statistics, only those trajectories that access the seam at least once (i.e., only those trajectories that get past the dynamical bottlenecks associated with T1 or T2 adiabatic saddle points) are included. The probability of undergoing a spin-forbidden transition at each seam crossing depends on the total energy, the local properties of the crossing seam, etc., but is always small (less than 0.005). Seam crossings therefore typically come in pairs, as the first seam crossing is associated with the formation of $^3CO_2$ and a second seam crossing is required to produce the most likely product, O + CO.

At 5000 K, 58% of T1 trajectories are trapped, at least temporarily, by the $^3CO_2$ well and access the S0/T1 seam more than twice: 42% access the seam exactly twice, 29% access the seam exactly four times, and the majority of the remaining trajectories access the seam more than four times with successive pairs of crossings exponentially less likely. A small number of

reactive trajectories access the seam an odd number of times. Much less trapping is observed for trajectories initiated on the T2 surface, which features a shallower $^3CO_2$ well than the T1 surface. At 5000 K, 87% of trajectories encounter the S0/T2 seam exactly twice, with the majority of the remaining trajectories encountering the seam exactly four times. For T1, the fraction of trapped trajectories increases significantly at lower temperatures. At 2000 K, for example, 16% of T1 trajectories that access the seam do so exactly twice, with the majority of the remaining trajectories accessing the seam four or more times. For T2, in contrast, the fraction of trapped trajectories is relatively insensitive to temperature. These results are consistent with the submerged surface crossing threshold for T1 and the positive surface crossing threshold for T2, as well as the shallower T2 well.

The paired seam crossings identified above might be used to motivate the "double passage" transition probabilities used in some statistical models for nonadiabatic kinetics.[31,32,75] The double passage approximation incorporates two effects: First, it accounts for passage through the seam in both directions. (In an adiabatic TST calculation, on the other hand, flux only in the reactive direction is counted.) Second, it accounts for depletion of population at the second pass, i.e., if the probability of a nonadiabatic transition at the first pass is $P_1$, the probability of crossing the seam a second time is reduced by $(1–P_1)$. The double passage formulation is most readily motivated by considering a one-dimensional (e.g., diatomic) system. In one dimension, if $P_1$ is not too large,[76] both of the effects identified above are accounted for properly via the double passage method and the system accesses the seam (which in one dimension is a single geometry) at the same geometry. For polyatomic systems, the accuracy of the double passage method is less clear, despite the paired crossings noted above. In the present calculations, a significant fraction of trajectories access the seam more than twice, which would result in probabilities further reduced by $(1–P_1)(1–P_2)$, $(1– P_3)(1–P_2)(1–P_3)$, etc. at each pass. These "more than double passage" effects (which do not arise in one dimension) are not included in the "double passage" approximation. (If $P_i$ is small enough such that depletion may be neglected, golden rule formulations of nonadiabatic kinetics may be more appropriate than the double passage approach.[77]) Furthermore, we note that the paired seam crossings identified above are not typically associated with similar locations on the crossing seam. As mentioned above, the local nonadiabatic transition probability can vary significantly along the crossing seam. In general, the nonlocal (history-dependent, dynamical) effects identified here are difficult

to incorporate into statistical theories. The present trajectory calculations explicitly include these nonlocal population-depletion and history-dependent effects.

Fig. 3 shows the distribution of the geometries where 5000 K ensembles of 2000 CSDM trajectories encounter the S0/T1 and S0/T2 crossing seams as a function of $M$, where $M = 1$ for each trajectory's first encounter with the crossing seam, $M = 2$ for each trajectory's second encounter, etc. To make Fig. 3, a generalized seam coordinate $s$ was defined that describes the location each trajectory's encounters with the curved crossing seam (see Fig. 1):

$$s = \pm\sqrt{\frac{(R-R_0)^2}{\delta R^2} + \frac{(\theta-\theta_0)^2}{\delta\theta^2}} \qquad (15)$$

where $(R_0, \theta_0) = (1.71\ \text{Å}, 121^\circ)$ is a reference geometry, $\delta R$ and $\delta\theta$ are scaling factors that bound the magnitudes of each term to 1, and the sign of $s$ is determined by the sign of $\theta - \theta_0$. The S0/T1 MSX has a value of $s = -0.43$. Regions of the seam close to the T1 saddle point have values of $s$ near 0. For S0/T2, the MSX has a value of $s$ near zero, which is also close to the T2 saddle point.

As shown in Fig. 1(a), the geometries associated with the initial seam crossing ($M = 1$) are greatly affected by the preceding saddle point, with a distribution clustered near $s = 0$ (near the T1 saddle point). The distribution of geometries at the second crossing ($M = 2$) is clustered closer to the MSX with $s = -0.35$. Subsequent pairs of seam crossings appear more and more statistical and peaked near $s = -0.4$ with oscillating minor contributions near $s = 0$. Together these features give rise to the broad statistical distribution for $M > 2$ shown in Fig. 3(a). We may generally associate the initial seam crossing with a direct nonstatistical mechanism and later seam crossings with an indirect statistical mechanism. The two mechanisms differ in the distributions of their seam crossings geometries, and, notably, these differences in seam crossing geometries give rise to different average local (i.e., per-crossing) nonadiabatic transition probabilities. These differences are principally due to variations in the spin–orbit coupling strength along the seam (cf. Fig. 1), although they arise from other differences in the local crossing seam, as well. The direct ($M = 1$) encounters with the crossing seam have larger spin–orbit coupling strengths, on average, than those associated with the indirect mechanism. Specifically, the average value of $\varepsilon_1$ for $s \approx 0$ is 65 $\text{cm}^{-1}$, whereas the average value near $s = -0.4$ is 47 $\text{cm}^{-1}$. These differences, along with other differences in the local seam properties, give rise to per-crossing nonadiabatic transition probabilities that are ~2x larger near $s = 0$ than near $s = -0.4$. At 5000 K, the direct mechanism accounts for only 20% of total seam crossings, however,

such that the direct mechanism accounts for only 33% of the total spin-forbidden rate despite its larger per-crossing transition probability. As mentioned above, the relative importance of the direct mechanism decreases at lower temperatures for T1.

Fig. 3(b) shows seam crossing statistics for the S0/T2 seam and for 2000 5000 K trajectories initiated on the T2 surface. For this surface, the saddle point is close to the MSX (cf. Fig. 1) such that the distributions for $M = 1$, 2 and > 2 are all peaked near $s = 0$. As mentioned above, relatively fewer trajectories are trapped in the T2 well than the T1 well, and the total spin-forbidden dynamics is dominated by the first and second seam crossings for T2. We could again associate the first seam crossing ($M = 1$) with a direct mechanism for spin-forbidden reactions on the T2 surface (nearly half of seam crossings would be so assigned), but in this case both the direct and indirect mechanisms have similar seam crossing geometry distributions and so the distinction between indirect and direct mechanisms is less important.

Statistical assumptions about the distribution of seam crossings would therefore not introduce significant errors for either triplet state, but this is not necessarily a general result. In fact, for the two cases considered here, the statistical assumption is accurate for different reasons. For T1, the triplet well is deep enough to trap a significant enough fraction of the trajectories, such that the trapped statistical trajectories outnumber the initial direct seam crossings. For T2, on the other hand, the triplet well does not significantly delay the trajectories and nearly half of the total seam crossings are "direct" ones. However, the S0/T2 MSX happens to be close to the T2 saddle point, such that the direct and indirect geometry distributions are similar, with similar per-crossing nonadiabatic transition probabilities.

Overall, the present dynamical picture is similar to the one proposed by Hwang and Mebel[6] based on their characterization of static properties of the S0/T1 crossing seam, but differs in some important details. Most notably, the present dynamical picture suggests that the relative importance of the direct and indirect mechanisms depends on the depth of the transient well and on the similarity or difference of the saddle point and MSX structures.

The above discussion highlights the importance of including geometry dependence in the spin–orbit coupling surface. If the spin–orbit coupling surfaces were instead assumed to be independent of geometry (which is a common assumption in the literature) and assigned the values calculated at the MSX geometries, the overall spin-forbidden rate coefficients would be reduced by a factor of ~2.

Some statistical treatments of spin-forbidden dynamics treat the MSX similarly to a saddle point, with the crossing seam playing the role of the transition state dividing surface dynamical bottleneck. Within this picture, one is tempted to employ an analog of UST[78] in the present case, where one transition state is associated with the conventional saddle point on the triplet surface and the other is given by the MSX. Miller's UST describes the total rate coefficient for a system encountering two transition states in succession as[78] $N^{-1} = N_1^{-1} + N_2^{-1} - N_x^{-1}$. The derivation of UST recognizes that each transition state is local dynamical bottleneck (a local minimum in the nuclear flux) with values $N_1$ and $N_2$. When two such dynamical bottlenecks are in succession along some reaction coordinate, there is necessarily a maximum in the flux, $N_x$, associated with some intermediate geometry, most likely a well. If the intermediate well is "deep" enough, statistical assumptions about branching between the two adjacent transition states are expected to be good, $N_x^{-1} \to 0$, and eq 16 reduces to the expected statistical two transition state model.[79] When the well is shallow, however, the magnitude of $N_x^{-1}$ may become comparable to $N_1^{-1}$ or $N_2^{-1}$, such that the UST rate reduces to $N_1$ or $N_2$, whichever is rate limiting. When one of the "transition states" is a crossing seam instead of a conventional transition state, the formal foundation of the UST model breaks down. An MSX is not associated with any local minimum in the nuclear flux, and one cannot therefore rely on the appropriate reduction of UST to the two limits discussed above.

More generally, Wigner's fundamental assumption of TST associates the transition state with a local minimum in the nuclear flux.[80] The formal equivalence of TST with full-dimensional classical dynamics relies on the fact that once the flux through the transition state dividing surface is fully minimized, dynamical recrossing is minimized to zero, and *every state on the transition state dividing surface reacts with unit probability*. This fundamental property of classical dynamics gives rise to the variational principle in TST and to useful and accurate applications of TST for molecular systems. For spin-forbidden dynamics, in contrast, the probability of reaction at the seam is not unity and is in fact very small (the transition is forbidden, after all). "Recrossing" is indeed often required for appreciable spin-forbidden rates. The violation of the fundamental assumption of TST for spin-forbidden reactions gives rise to the nonlocal nonadiabatic dynamics discussed above (i.e., the breakdown of the double passage assumption in polyatomic systems), makes nonstatistical effects more likely than in

electronically adiabatic reactions, and cautions against the quantitative application of UST-like approaches. While statistical formulations of spin-forbidden (or more generally electronically nonadiabatic) dynamics may be practically useful, we emphasize that these formulations do not share the formal foundations of TST. Further critical evaluation of nonadiabatic statistical models may be required to enable quantitative predictions with these methods. The formal distinction between TST and nonadiabatic statistical theories has been previously emphasized by Miller.[77]

## IV. Summary and conclusions

The spin-forbidden kinetics and dynamics of the reaction O + CO → $CO_2$ was characterized theoretically. A global full-dimensional spin–orbit-coupled representation of the lowest-energy singlet and the two lowest-energy triplet states was developed based on nearly full valence dw-MRCI/CBS calculations and using the IMLS surface fitting method. The resulting potential energy surfaces were shown to agree very well with available experimental properties for $CO_2$ and CO. Geometry dependence was explicitly included in the calculated and fitted spin–orbit coupling surfaces. The magnitude of the spin–orbit coupling was shown to vary from 45–80 $cm^{-1}$ along the crossing seams.

The association kinetics was calculated using the CSDM method, which is a previously validated non-Born–Oppenheimer molecular dynamics (i.e., semiclassical coupled-states trajectory) method. Both triplet states were found to contribute non-negligibly to the total association rate coefficient. The total CSDM rate coefficient is 7–35x larger than the value used in many combustion kinetic models. A detailed analysis of potential sources of error in the present calculations was presented in the Appendix. The present calculations may be assigned an error of 40%, arising principally from the calculated spin–orbit coupling strength. The present results were found to be somewhat sensitive to choice of the electronic decoherence model used in the non-Born–Oppenhiemer trajectory calculations. The CSDM method features an explicit treatment of electronic decoherence, which was previously validated against quantum scattering calculations and was again tested here against a semicalssical model based on the short-time behavior of wave packets. We note that other semiclassical trajectory methods either neglect electronic decoherence or use other (sometimes simpler) models.

Dynamical details of the CSDM trajectories revealed distinct direct (nonstatistical) and indirect (statistical) mechanisms associated with different distributions of seam crossings. The direct mechanism features seam crossings shaped by the preceding saddle point, whereas the indirect mechanism features statistical distributions of seam crossings. Similar nonstatistical effects are likely generally important for spin-forbidden systems, although for the present system the application of an entirely statistical model would not lead to significant errors. The general appropriateness of statistical models for treating the inherently nonlocal dynamics of spin-forbidden processes was also discussed.

**Appendix. The accuracy of the present theoretical kinetics calculations**

To estimate the accuracy of the present classical description of the nuclear dynamics, electronically adiabatic rate coefficients for $^3O + CO \rightarrow {}^3CO_2$ for the T1 and T2 triplet states were each calculated three ways: via classical trajectories and the classical initial conditions described above ($k^{c}_{dyn}$), via classical rigid rotor–harmonic oscillator (RRHO) variational transition state theory (TST) ($k^{c}_{TST}$), and via quantum mechanical RRHO variational transition state theory ($k^{q}_{TST}$).[24] None of these calculations included tunneling corrections. The variational TST calculations were performed using POLYRATE,[81] with stretch/stretch/bend curvilinear coordinates[82] and the re-orientation of dividing surfaces[83] (RODS) method. The ratio

$$\kappa_{dyn}(T) = k^{c}_{dyn} / k^{c}_{TST} \tag{17}$$

defines a dynamical correction to TST due to trajectory recrossing[24,84] and also includes the effect of vibrational anharmonicity. For both T1 and T2, $\kappa_{dyn}$ = 0.92–1.0 for $T$ = 1000–5000 K, where the small deviation from unity increases with temperature.

The ratio

$$C_q(T) = k^{q}_{TST} / k^{c}_{TST} \tag{18}$$

defines a correction to the trajectory-based rate coefficients that arises from the use of classical partition functions and thresholds. This can be seen more clearly by substituting into eq 6 the classical and quantal bimolecular TST expressions, i.e.,

$$k^{z}_{TST} = \frac{k_B T}{h} \frac{Q^{\neq}_{z}}{Q^{R}_{z}} \exp(-V^{\neq}_{z} / k_B T), \tag{19}$$

where $z$ = "q" or "c", $k_B$ is Boltzmann's constant, $Q_z^{\neq}$ is the pseudopartition function for the transition state, $Q_z^{\mathrm{R}}$ is the total partition function for the reactants, the partition functions are defined relative to their classical or quantal (i.e., zero point inclusive) thresholds, and $V_z^{\neq}$ is the classical or quantal barrier height. One can then write eq 18 as

$$C_q(T) = \frac{Q_{\mathrm{c}}^{\mathrm{R}} / \tilde{Q}_{\mathrm{q}}^{\mathrm{R}}}{Q_{\mathrm{c}}^{\neq} / \tilde{Q}_{\mathrm{q}}^{\neq}} \equiv \frac{C_q^{\mathrm{R}}}{C_q^{\neq}} \tag{20}$$

where the over-tilde indicates that the quantal partition functions are evaluated relative to the classical reference energies. By construction, the correction terms $C_q^{\ddagger}$ and $C_q^{\mathrm{R}}$ each tend to unity at high temperatures, as the classical limit is approached. In general, one expects the classical description to be poor for molecules at low and moderate temperatures (and even sometimes at high temperatures for high-frequency vibrations, for example). The terms in eq 20 may be readily evaluated. For the present system, $C_q^{\ddagger}$ and $C_q^{\mathrm{R}}$ are significant at 300 K (15 and 17, respectively), are non-negligible at 1000 K (1.4 and 1.5, respectively), and are within 10% of unity for temperatures above 2000 K; i.e., this heavy-atom system is well represented as a classical system for temperatures greater than ~2000 K. The use of classical mechanics for the *overall rate coefficient*, however, is much more accurate, even at low temperatures, due to the significant cancellation in the ratio of $C_q^{\ddagger}$ and $C_q^{\mathrm{R}}$. The overall quantal correction to the predicted rate coefficient $C_q$ is only 17% at 300 K and is less than 2% at temperatures above 1000 K. Classical rate coefficients for the present system may therefore be expected to be very accurate at low temperatures—despite the fact that the partition functions themselves may not be near their classical limits—due to cancellation of the quantal corrections for the reactants and at the transition state. *Some* cancellation is expected in general but the present significant cancellation down to very low temperatures relies on the fact that one of the harmonic transition state frequencies is very close to the reactant CO frequency (both near 2100 $\mathrm{cm}^{-1}$) and the other transition state frequency (322 $\mathrm{cm}^{-1}$) is small enough to be well approximated classically.

The above analysis considered the adiabatic dynamics associated with the conventional adiabatic bottlenecks (saddle points) on the triplet surfaces. The spin-forbidden kinetics governing reaction 1 is sensitive to the state densities at the crossing seams, where one cannot necessarily rely on the excellent cancellation discussed above. Regardless, as noted above, the partition functions themselves are close to their classical limits above 2000 K. We estimate that

the error due to classical nuclear dynamics is less than 10% for this system for temperatures above 2000 K and may be somewhat larger at 1000 K.

Next we consider the accuracy of the CSDM method for describing the electronically nonadiabatic dynamics. The CSDM method has been tested against quantum scattering calculations for product branching and for internal energy distributions for a series of atom-diatom reactions featuring a variety of electronically nonadiabatic interaction types.[56,57,58] The results of these tests have been recently summarized.[27,59] The overall relative error in the CSDM method was found to be only 23%, averaged over several systems and several observables. The errors obtained in these previous tests include errors arising from both the nuclear and electronically nonadiabatic dynamics, and as discussed above, one expects the nuclear dynamics of the present system to be well approximated classically. We therefore assign an overall error of ~20% to the CSDM method for the present application.

Historically, errors arising from the potential energy surface have dominated the overall error in many kinds of dynamics calculations. The high general accuracy of the dw-MRCI+Q/CBS method for small systems like $CO_2$ and the very small fitting error associated with the ILMS method significantly minimizes the error in the present calculations arising from the potential energy surfaces. These errors are likely very small, even relative to the small error assigned to the CSDM method. For example, a 0.2 kcal/mol error in a barrier height (this is the *maximum* fitting error of the present IMLS application for the stationary points listed in Table 1) introduces only a 10% error into a TST calculation at 1000 K and a 2% error at 5000 K.

The most significant source of error in the present calculation is likely the calculated spin-orbit coupling strengths. It is difficult to estimate the error associated with the Breit-Pauli model for $H_{SO}$ described in Sec. II.A and used to calculate $\varepsilon_1$ and $\varepsilon_2$. Our own[85] and earlier[50,51] studies of the accuracy of this model for halogen atoms suggest that, for the lighter halogens at least, the error is only a few percent. The absolute magnitude of the error in these studies was tens or even hundreds of $cm^{-1}$, however, which is significant relative to the magnitude of $\varepsilon_1$ and $\varepsilon_2$. However, as mentioned in section II.A. above, calculations for atomic oxygen using the methods employed in this study were found to be highly accurate. Our analysis in Sec. II.A showed some sensitivity to the choice of quantum chemistry method (primarily for significantly smaller active spaces). We may reasonably assign an error of ~20% arising from the Breit-Pauli

model, the choice of quantum chemistry method, and from the IMLS fitting error. Such an error would contribute a 40% error to the predicted spin-forbidden rate coefficient.

We confirmed that the present dynamics are close to the perturbative limit with respect to $\varepsilon$ (except for $k_S^{\mathrm{T1}}$ for $T < 2000$ K) such that if more accurate values of $\varepsilon_1$ and $\varepsilon_2$ could be obtained, the present results could be corrected via the simple relation

$$k'_S(T) = k_S^{\mathrm{T1}}(T)\left(\frac{\varepsilon'_1}{\varepsilon_1}\right)^2 + k_S^{\mathrm{T2}}(T)\left(\frac{\varepsilon'_2}{\varepsilon_2}\right)^2 \qquad (21)$$

where the primes indicate improved spin-orbit coupling strengths evaluated at some reference geometries (e.g., at the MSXs).


## Acknowledgments

We thank Leonid Sheps and John Keifer for helpful conversations regarding the experimental kinetics literature. A. W. J. is supported by the Division of Chemical Sciences, Geosciences, and Biosciences, Office of Basic Energy Sciences, U.S. Department of Energy. Sandia is a multiprogram laboratory operated by Sandia Corporation, a Lockheed Martin Company, for the United States Department of Energy under Contract No. DE-AC04-94-AL85000. R. D. is supported by the Office of Basic Energy Sciences, Division of Chemical Sciences, U.S. Department of Energy under Contract No. DE-SC0010616.

Table 1. Experimental, fitted, and calculated **energies**[a] (kcal/mol), *geometries* ($R$/Å, $R'$/Å, $\theta$/°), and harmonic frequencies ($cm^{-1}$)

| Stationary point | Experimental[b] | IMLS | dw-MRCI+Q/CBS | Ref. 6[c] | Ref. 7[d] | Ref. 10[e] |
|---|---|---|---|---|---|---|
| $^3O + CO$ | **(0.0)**[f]<br>*1.128*<br>2170 | **0.0**[f] | **0.0 (0.0)**[f]<br>*1.127* | **0.0**<br>*1.15*<br>2119 | **0.0** | **0.0** |
| $^1O + CO$ | **(45.38)**<br>*1.128*<br>2170 | | **44.82 (45.05)**[f]<br>*1.127* | **51.1**<br>*1.15*<br>2119 | | |
| $CO_2$ | **(–125.8)**<br>*1.162, 1.162, 180.0*<br>667.4(x2), 1333, 2349 | **–130.0 (–125.9)**<br>*1.160, 1.160, 180.0*<br>665.3(x2), 1361, 2402 | **–130.1**<br>*1.161, 1.161, 180.0* | **–129.1**<br>*1.17, 1.17, 180*<br>636(x2), 1333, 2447 | | |
| $CO_2$ ($^3$A') | | **–21.26**<br>*1.241, 1.242, 118.6*<br>584.0, 1113, 1426 | **–21.16**<br>*1.242, 1.242, 118.0* | **–18.6**<br>*1.20, 1.33, 121*<br>601, 1092, 2348 | **–22**<br>*1.26, 1.26, 118*<br>540, 1110, 1310 | **–20.5**<br>*1.251, 1.251, 118.5*<br>622, 752, 1414 |
| $CO_2$ ($^3$A") | | **–5.424**<br>*1.248, 1.256, 128.1*<br>497.6, 875.2, 1312 | **–5.350**<br>*1.251, 1.251, 127.2* | | **–5.4**<br>*1.27, 1.27, 127*<br>580, 880, 1040 | **–5.42**<br>*1.261, 1.261, 127.4* |
| $[^3O + CO \rightleftarrows {}^3CO_2]^‡$ ($^3$A') | | **6.461**<br>*1.134, 1.920, 119.3*<br>489.2*i*, 321.8, 2098 | **6.539**<br>*1.134, 1.92, 120.8* | **5.9**<br>*1.16, 1.81, 122*<br>663*i*, 317, 2067 | **5**<br>*1.16, 2.0, 112* | |
| $[^3O + CO \rightleftarrows {}^3CO_2]^‡$ ($^3$A") | | **7.805**<br>*1.135, 1.863, 125.9*<br>423.5*i*, 322.5, 2087 | **7.979**<br>*1.136, 1.86, 126.2* | | **7**<br>*1.16, 1.85, 122* | |
| S0/T1 MSX ($^3$A') | | **–17.06**<br>*1.255, 1.255, 106.6*<br>1025, 1234 | | **–10.0**<br>*1.25, 1.25, 110* | | |
| S0/T2 MSX ($^3$A") | | **6.970**<br>*1.143, 1.740, 121.6*<br>440.3, 1996 | | | | |

[a]Electronic energies are reported relative to $^3O + CO$, with spin-orbit- and zero-point-corrected energies given in parenthesis.
[b]NIST Webbook[40]
[c]Several levels of theory were considered by Hwang and Mebel.[6] Here the average of their QCISD(T)/6-311+G(3df)//CASSCF/6-311+G(3df) energies for MSX ($^3$A') (their MSX1) and their G2(MP2) energies for the other stationary points are shown.
[d]CASSCF-MP2/6-31+G(d) with a (12e,10o) active space
[e]MRCI//CASSCF with a (16e,12o) active space and a custom basis set
[f]The CO + O asymptote is not explicitly included in the IMLS fit. The asymptotic triplet energy is zero by construction.

Table 2. Spin–orbit coupling strengths for several levels of theory calculated at geometries near the crossing seam minima

| Method | Basis set | Active space | State averaging | $\varepsilon_1$, $cm^{-1}$ | $\varepsilon_2$, $cm^{-1}$ |
|---|---|---|---|---|---|
| IMLS[a] | n/a | n/a | n/a | 47.94 | 63.08 |
| CASSCF | aug-cc-pVQZ | (16e,12o) | dynamic[b] | 53.36 | 56.44 |
| CASSCF | aug-cc-pVQZ | (12e,10o) | dynamic | 46.69 | 56.47 |
| CASSCF | aug-cc-pVQZ | (10e,8o) | dynamic | 30.45 | 56.71 |
| CASSCF | aug-cc-pVQZ | (8e,6o) | dynamic | 20.60 | 53.61 |
| CASSCF | aug-cc-pVTZ | (12e,10o) | dynamic | 46.00 | 55.20 |
| CASSCF | aug-cc-pVDZ | (12e,10o) | dynamic | 44.03 | 52.95 |
| CASSCF | aug-cc-pVQZ | (12e,10o) | fixed[c] | 49.88 | 63.79 |
| MRCI | aug-cc-pVDZ | (12e,10o) | dynamic | 44.61 | 50.48 |

[a]The IMLS coupling surfaces were fit using the dynamically-weighted CASSCF/aug-cc-pVQZ (12e,10o) method.

[b]The dynamic weighting (dw) scheme was used.

[c]Equal fixed weights were used for the two lowest singlet and the two lowest triplet states.

**Figure Captions**

Fig 1. IMLS surfaces for (a) $V_{S0}$, (b) $V_{T1}$, (c) $\varepsilon_1$, (d) $V_{T2}$, and (e) $\varepsilon_2$. The remaining CO distance was optimized with respect to $V_S$ for (a), $V_{T1}$ for (b) and (c), and $V_{T2}$ for (d) and (e). For (a), (b), and (d), the contours lines indicate the O + CO zero of energy (bold), 10 kcal/mol contour increments (solid), and 1 kcal/mol contour increments from 1–9 kcal/mol (dashed). For (c) and (d), the contour spacing is 10 $cm^{-1}$, and some contours are labeled. The S0/T1 and S0/T2 crossing seams are shown in red and blue, respectively. The triplet saddle points and the minima on the crossing seams (MSXs) are labeled with 'o' and 'x', respectively.

Fig. 2. Rate coefficient for reaction 1 calculated using the CSDM method (symbols) for trajectories initiated on the T1 (red squares) and T2 (blue triangles) surfaces. The total calculated rate coefficient is shown as black circles. The modified Arrhenius fits in eqs 9–11 are shown as the associated solid lines. Two sigma statistical error bars are shown and are sometimes smaller than the symbols. The rate coefficient from Ref. 2 is shown as a thick black line.

Fig 3. Seam crossing statistics for 2000 CSDM trajectories at 5000 K initiated on the (a) T1 and (b) T2 surfaces. The seam coordinate *s* is defined in eq 15.

**Figure 1**

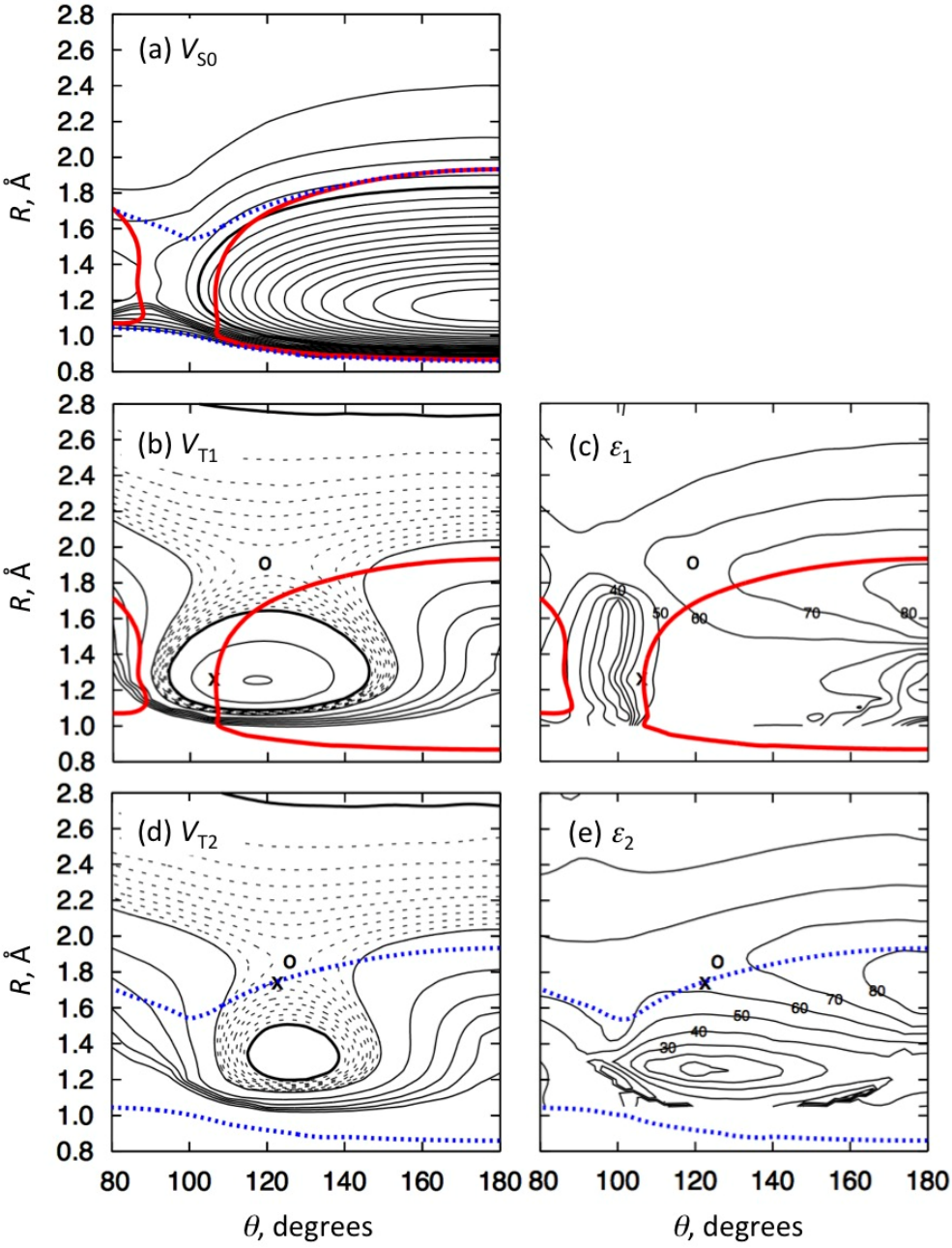


Fig 1. IMLS surfaces for (a) $V_{S0}$, (b) $V_{T1}$, (c) $\varepsilon_1$, (d) $V_{T2}$, and (e) $\varepsilon_2$. The remaining CO distance was optimized with respect to $V_S$ for (a), $V_{T1}$ for (b) and (c), and $V_{T2}$ for (d) and (e). For (a), (b), and (d), the contours lines indicate the O + CO zero of energy (bold), 10 kcal/mol contour increments (solid), and 1 kcal/mol contour increments from 1–9 kcal/mol (dashed). For (c) and (d), the contour spacing is 10 $cm^{-1}$, and some contours are labeled. The S0/T1 and S0/T2 crossing seams are shown in red and blue, respectively. The triplet saddle points and the minima on the crossing seams (MSXs) are labeled with 'o' and 'x', respectively.

**Figure 2**

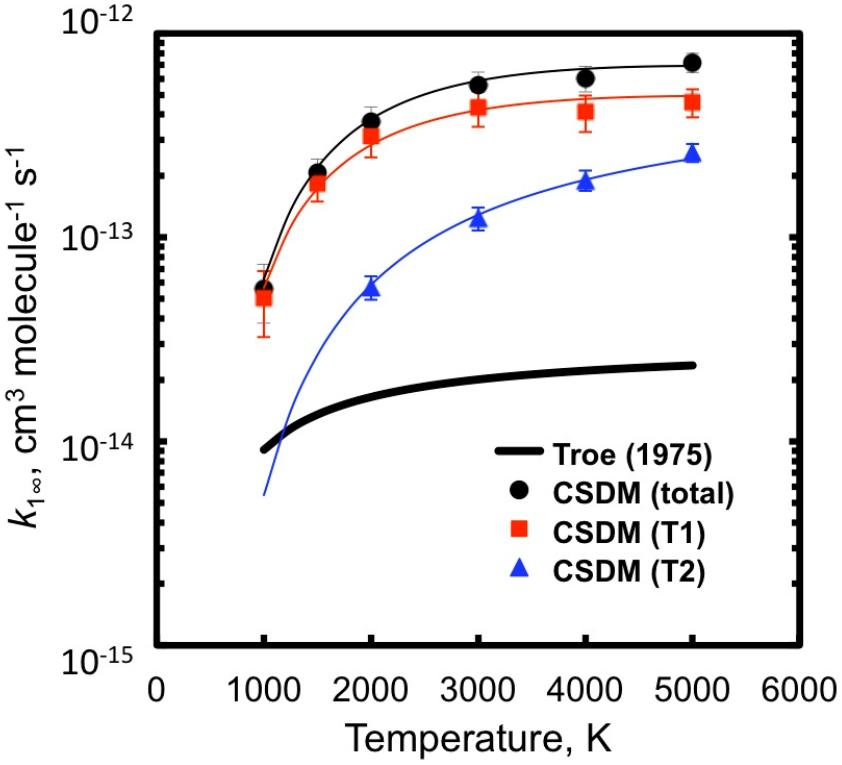


Fig. 2. Rate coefficient for reaction 1 calculated using the CSDM method (symbols) for trajectories initiated on the T1 (red squares) and T2 (blue triangles) surfaces. The total calculated rate coefficient is shown as black circles. The modified Arrhenius fits in eqs 9–11 are shown as the associated solid lines. Two sigma statistical error bars are shown and are sometimes smaller than the symbols. The rate coefficient from Ref. 2 is shown as a thick black line.

**Figure 3**

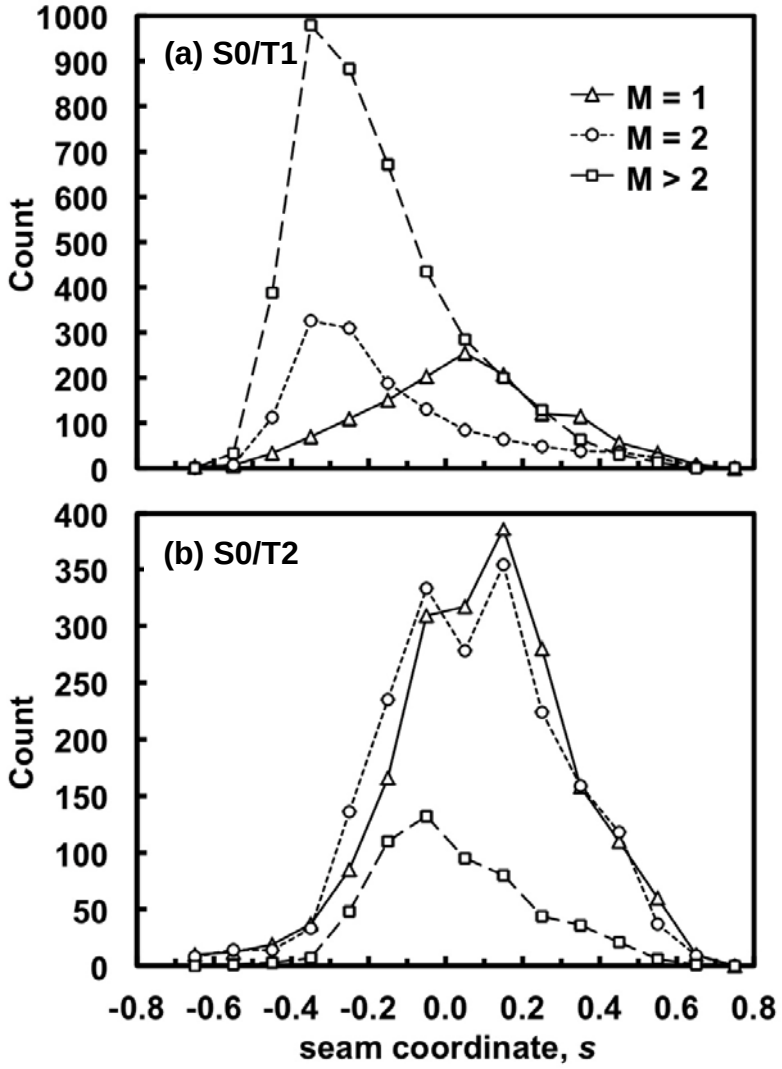


Fig 3. Seam crossing statistics for 2000 CSDM trajectories at 5000 K initiated on the (a) T1 and (b) T2 surfaces. The seam coordinate *s* is defined in eq 15.

## References


[1] M. T. Allen, R. A. Yetter, and F. L. Dryer, *Combus. Flame* **109**, 449 (1997).

[2] J. Troe, *Fifteenth Symp. (Int.) Combust.* **15**, 667 (1975).

[3] P. R. Westmoreland, J. B. Howard, J. P. Longwell, and A. M. Dean, *AIChE J.* **32**, 1971 (1986).

[4] S. G. Davis, A. V. Joshi, H. Wang, and F. Egolfopoulos, *Proc. Combust. Inst.* **30**, 1283 (2005).

[5] A. M. Starik, N. S. Titova, A. S. Sharipov, and V. E. Kozlov, *Combust. Explosion Shock Waves* **46**, 491 (2010).

[6] D.-Y. Hwang and A. M. Mebel, *Chem. Phys.* **256**, 169 (2000).

[7] M. Braunstein and J. W. Duff, *J. Chem. Phys.* **112**, 2736 (2000).

[8] A. L. Brunsvold, H. P. Upadhyaya, J. Zhang, R. Cooper, T. K. Minton, M. Braunstein, and J. W. Duff, *J. Phys. Chem. A* **112**, 2192 (2008).

[9] S. Yu. Grebenshchikov, J. Chem. Phys. **138**, 224106 (2013).

[10] A. Spielfiedel, N. Feautrier, C. Cossart-Magos, G. Chambaud, P. Rosmus, H.-J. Werner, and P. Botschwina, *J. Chem. Phys.* **97**, 8382 (1992).

[11] M. A. Oehlschlaeger, D. F. Davidson, J. B. Jeffries, and R. K. Hanson, *Z. Phys. Chem.* **219**, 93 (2005).

[12] S. Saxena, J. H. Kiefer, and R. S. Tranter, *J. Phys. Chem. A* **111**, 3884 (2007).

[13] Numerous earlier experimental studies exist; see, e.g., Ref. 12 for a critical review of existing experimental results.

[14] J. Troe, *J. Chem. Phys.* **66**, 4745 (1977).

[15] J. Troe, *J. Chem. Phys.* **66**, 4758 (1977).

[16] W. A. Hardy, H. Vasatko, H. Gg. Wagner, and F. Zabel, *Ber. Busen-Ges. Phys. Chem.* **78**, 76 (1974).

[17] Wagner, H. Gg.; Zabel, F. *Ber. Bunsen-Ges. Phys. Chem.* **78**, 705 (1974).

[18] A. P. Zuev and A. Y. Starikovskii, *Khimicheskaya Fizika*, **11**, 1518 (1992).

[19] E. C. Y. Inn and J. M. Heimerl, *J. Atoms. Sci.* **28**, 838 (1971).

[20] A. Stolow and Y. T. Lee, *J. Chem. Phys.* **98**, 2066 (1993).

[21] I. C. Lu, J. J. Lin, S. H. Lee, Y. T. Lee, and X. M. Yang, *Chem. Phys. Lett.* **382,** 665 (2003).

[22] Z. Chen, F. Liu, B. Jiang, X. Yang, and D. H. Parker, *J. Phys. Chem. Lett.* **1**, 1861 (2010).

[23] S. Yu. Grebenshchikov, *J. Chem. Phys.* **138**, 224107 (2013).

[24] A. Fernández -Ramos, J. A. Miller, S. J. Klippenstein, D. G. Truhlar, *Chem. Rev.* **106**, 4518 (2006).

[25] L. B. Harding, S. J. Klippenstein, and A. W. Jasper, *Phys. Chem. Chem. Phys.* **9**, 4055 (2007).

[26] J. C. Tully, in *Modern Methods for Multidimensional Dynamics Calculations*, edited by D. L. Thompson (World Scientific, Singapore, 1998), p. 34.

[27] A. W. Jasper, S. Nangia, C. Zhu, and D. G. Truhlar, *Acc. Chem. Res.* **39**, 101 (2006).

[28] C. Zhu, S. Nangia, A. W. Jasper, and D. G. Truhlar, *J. Chem. Phys.* **121**, 7658 (2004).

[29] H.-D. Meyer and W. H. Miller, *J. Chem. Phys.* **70**, 3214 (1979).

[30] J. C. Tully, *J. Chem. Phys.* **93**, 1061 (1990).

[31] Q. Cui, K. Morokuma, J. M. Bowman, and S. J. Klippenstein, *J. Chem. Phys.* **110**, 9469 (1999).

[32] J. N. Harvey, *Phys. Chem. Chem. Phys.* **9**, 331 (2007).

[33] R. Dawes, A. F. Wagner, and D. L. Thompson *J. Phys. Chem. A.* **113**(16) 4709-4721 (2009).

[34] A. Li, A. Xie, R. Dawes, A. W. Jasper, J. Ma, and H. Guo, *J. Chem. Phys.* **133**, 144306 (2010).

[35] A. J. Binder, R. Dawes, A. W. Jasper, J. P. Camden, *J. Phys. Chem. Lett.* **1**, 2940, (2010).

[36] R. Dawes, X.-G. Wang, A. W. Jasper, T. Carrington Jr., *J. Chem. Phys.* **133**, 134304 (2010).

[37] M. P. Deskevich, D. J .Nesbitt, and H. J. Werner, *J. Chem. Phys.* **120**, 7281 (2004).

[38] R. Dawes, A. W. Jasper, C. Tao, C. Richmond, C. Mukarakate, S. H. Kable, and S. A. Reid, *J. Phys. Chem. Lett.* **1**, 641 (2010)

[39] T. Helgaker, P. Jorgensen, and J. Olsen, *Molecular Electronic Structure Theory* (Wiley, New York, 2000).

[40] NIST Chemistry WebBook, NIST Standard Reference Database Number 69, Eds. P.J. Linstrom and W.G. Mallard, National Institute of Standards and Technology, Gaithersburg MD, 20899, http://webbook.nist.gov.

[41] B. J. Barker, I. O. Antonov, J. M. Merritt, V. E. Bondybey, M. C. Heaven, R. Dawes, *J. Chem. Phys.* **137**, 214313 (2012).

[42] C. Tao, C. Richmond, C. Mukarakate, S. H. Kable, G. B. Bacskay, E. C. Brown, R. Dawes, P. Lolur and S. A. Reid, *J. Chem. Phys.* **137**, 104307 (2012).

[43] R. Dawes, P. Lolur, J. Ma and H. Guo, *J. Chem. Phys.* **135**, 081102 (2011).

[44] A. Berning, M. Schweizer, H.-J. Werner, P. J. Knowles, and P. Palmier, *Mol. Phys.* **98**, 1823 (2000).

[45] MOLPRO, version 2012.1, a package of *ab initio* programs, H.-J. Werner, P. J. Knowles, G. Knizia, F. R. Manby, M. Schütz, P. Celani, T. Korona, R. Lindh, A. Mitrushenkov, G. Rauhut, K. R. Shamasundar, T. B. Adler, R. D. Amos, A. Bernhardsson, A. Berning, D. L. Cooper, M. J. O. Deegan, A. J. Dobbyn, F. Eckert, E. Goll, C. Hampel, A. Hesselmann, G. Hetzer, T. Hrenar, G. Jansen, C. Köppl, Y. Liu, A. W. Lloyd, R. A. Mata, A. J. May, S. J. McNicholas, W. Meyer, M. E. Mura, A. Nicklass, D. P. O'Neill, P. Palmieri, D. Peng, K. Pflüger, R. Pitzer, M. Reiher, T. Shiozaki, H. Stoll, A. J. Stone, R. Tarroni, T. Thorsteinsson, and M. Wang, see http://www.molpro.net.

[46] M. R. Hoffmann and G. C. Schatz, *J. Chem. Phys.* **113**, 9456 (2000).

[47] B. Maiti and G. C. Schatz, *J. Chem. Phys.* **119**, 12360 (2003).

[48] T.-S. Chu, X. Zhang, and K.-L. Han, *J. Chem. Phys.* **122**, 214301 (2005).

[49] J. Zhao, *J. Chem. Phys.* **138**, 134309 (2013).

[50] A. Nicklass, K. A. Peterson, A. Berning, H.-J. Werner, and P. J. Knowles, *J. Chem. Phys.* **112**, 5642 (2000).

[51] A. Berning, M. Schweizer, H.-J. Werner, P. J. Knowles, and P. Palmieri, *Mol. Phys.* **98**, 1823 (2000).

[52] C. A. Mead and D. G. Truhlar, *J. Chem. Phys.* **77**, 6090, (1982).

[53] A. W. Jasper, S. N. Stechmann, and D. G. Truhlar, *J. Chem. Phys.* **116**, 5424 (2002); **117**, 10427(E) (2002).

[54] T. J. Martinez, *Acc. Chem. Res.* **39**, 119 (2006).

[55] C. Zhu, A. W. Jasper, and D. G. Truhlar, *J. Chem. Phys.* **120**, 5543 (2004).

[56] Y. L. Volobuev, M. D. Hack, M. S. Topaler, and D. G. Truhlar, *J. Chem. Phys.* **112**, 9716 (2002).

[57] A. W. Jasper, M. D. Hack, and D. G. Truhlar, *J. Chem. Phys.* **115**, 1804 (2001).

[58] A. W. Jasper and D. G. Truhlar, *J. Chem. Phys.* **122**, 044101 (2005).

[59] A. W. Jasper and D. G. Truhlar, in *Conical Intersections: Theory, Computation, and Experiment*, edited by W. Domcke, D. R. Yarkony, and H. Köppel (World Scientific, 2001).

[60] A. W. Jasper, C. Zhu, S. Nangia, and D. G. Truhlar, *Faraday Discuss. Chem. Soc.* **127**, 1 (2004).

[61] M. D. Hack and D. G. Truhlar, *J. Phys. Chem.* A **104**, 7917 (2000).

[62] O. V. Prezhdo and P. J. Rossky, *J. Chem. Phys.* **107**, 5863 (1997).

[63] D. G. Truhlar, in "Quantum Dynamics of Complex Molecular Systems," edited by D. A. Micha and I. Burghardt (Springer, Berlin, 2007), pp. 227–243.

[64] W. H. Miller, *J. Chem. Phys.* **136**, 210901 (2012).

[65] G. Granucci and M. Persico, *J. Chem. Phys.* **126**, 134114 (2007).

[66] T. Nelson, S. Fernandez-Alberti, A. E. Roitberg, and S. Tretiak, *J. Chem. Phys.* **138**, 224111 (2013).

[67] A. W. Jasper and D. G. Truhlar, *J. Chem. Phys.* **123**, 064103 (2005).

[68] R. Valero, D. G. Truhlar, and A. W. Jasper, *J. Phys. Chem.* **112**, 5756 (2008).

[69] H. C. Andersen, *J. Chem. Phys.* **1980**, *72*, 2348.

[70] D. G. Truhlar and J. T. Muckerman, in "Atom-Molecule Collision Theory: A Guide for the Experimentalist," edited by R. D. Bernstein (Plenum, New York, 1979), pp. 505–566.

[71] L. M. Raff and D. L. Thompson, in "Theory of Chemical Reaction Dynamics, Vol. 3," edited by M. Baer (CRC Press, Boca Raton, 1985), pp. 1–121.

[72] R. Schinke, "Photodissociation Dynamics" (Cambridge University Press, Cambridge, 1993).

[73] A. W. Jasper and D. G. Truhlar, *J. Chem. Phys.* **127**, 194306 (2007).

[74] A. W. Jasper and D. G. Truhlar, *Chem. Phys. Lett.* **369**, 60 (2003).

[75] J. B. Delos, *J. Chem. Phys.* **59**, 2365 (1973).

[76] A. J. Marks and D. L. Thompson, *J. Chem. Phys.* **96**, 1911 (1992).

[77] G. E. Zahr, R. K. Preston, and W. H. Miller, *J. Chem. Phys.* **62**, 1127 (1975).

[78] W. H. Miller, *J. Chem. Phys.* **65**, 2216 (1976).

[79] S. J. Klippenstein, L. R. Khundkar, A. H. Zewail, and R. A. Marcus, *J. Chem. Phys.* **89**, 4761 (1988).

[80] E. Wigner, *J. Chem. Phys.* **5**, 720 (1937).

[81] J. C. Corchado, Y.-Y. Chuang, P. L. Fast, W.-P. Hu, Y.-P. Liu, G. C. Lynch, K. A. Nguyen, C. F. Jackels, A. F. Ramos, B. A. Ellingson, B. J. Lynch, J. Zheng, V. S. Melissas, J. Villa, I. Rossi, E. L. Coitiño, J. Pu, T. V. Albu, R. Steckler, B. C. Garrett, A. D. Isaacson, and D. G. Truhlar, POLYRATE 9.7, University of Minnesota, Minneapolis, 2007. (See http://comp.chem.umn.edu/polyrate/)

[82] C. F. Jackels, Zhen Gu, and D. G. Truhlar, *J. Chem. Phys.* **102,** 3188 (1995).

[83] J. Villà and D. G. Truhlar, *Theor. Chem. Acc.* **97,** 317 (1997).

[84] J. Keck, *Discussions Faraday Soc.* **33**, 173 (1962).

[85] A. W. Jasper, S. J. Klippenstein, and L. B. Harding, *J. Phys. Chem. A* **114**, 5759 (2010).